Introducing novel electronic and magnetic properties in

PCCP
Physical Chemistry Chemical Physics

Accepted Manuscript

This article can be cited before page numbers have been issued, to do this please use: A. Bafekry, S. Farjami Shayesteh and F. M. Peeters , *Phys. Chem. Chem. Phys.*, 2019, DOI: 10.1039/C9CP03853A.

ROYAL SOCIETY OF CHEMISTRY

rsc.li/pccp

View Article Online
DOI: 10.1039/C9CP03853A

Introducing Novel Electronic and Magnetic Properties in C_3N Nanosheet by Defect Engineering and Atom Substitution

Asadollah Bafekry,*,†,‡ Saber Farjami Shayesteh,† and Francois M. Peeters‡

†*Department of Physics, University of Guilan, 41335-1914 Rasht, Iran*

‡*Department of Physics, University of Antwerp, Groenenborgerlaan 171, B-2020 Antwerp, Belgium*

E-mail: Bafekry.asad@gmail.com

Abstract

Using first-principles calculations the effect of topological defects, vacancies, Stone-Wales and anti-site and substitution of atoms, on the structure and electronic properties of monolayer C_3N are investigated. Vacancy defects introduce localized states near the Fermi level and a local magnetic moment. While pristine C_3N is an indirect semiconductor with 0.4 eV band gap, with substitution of O, S and Si atoms for C, it remains a semiconductor with band gap in the range 0.25-0.75 eV, while it turns into a metal with H, Cl, B, P, Li, Na, K, Be and Mg substitution. With F substitution, it becomes a dilute-magnetic semiconductor, while with Ca substitution it is a ferromagnetic-metal. When replacing the N host atom, C_3N turns into: metal (H, O, S, C, Si, P, Li and Be), ferromagnetic-metal (Mg), half-metal (Ca) and spin-glass semiconductor (Na and K). Moreover, the effects of charging and strain on the electronic properties of Na atom substitution in C_3N are investigated. We found that the magnetic moment decrease or increase depending on the type and size of strain (tensile or compression). Our study

View Article Online
DOI: 10.1039/C9CP03853A

shows how the band gap and magnetism in monolayer C_3N can be tuned by introducing defects and atom substitution. The so engineered C_3N can be a good candidate for future low dimensional devices.

Introduction

Graphene[1] as a two-dimensional material (2DM) with crystal lattice of carbon atoms, has recently attracted a lot of interest. 2DM forms a large family of materials involving various kinds of chemical elements showing unique properties quite distinct from their 3D bulk structures. Despite the fact that 2DM hold great potential for a wide range of applications, it will be necessary to modulate their intrinsic properties for real applications. Many approaches have been developed to modify the electronic and magnetic properties of 2DM. These methods involve substitution of atoms, defect engineering, surface functionalization and applying strain and/or electric field. Several computational studies have been conducted to investigate adatom and molecule adsorption on 2D monolayers[2–11] and substitution of atoms.[12–14] Substitution of atoms into 2DM is of fundamental importance in order to tailor their electronic and magnetic properties, which are useful for numerous applications such as energy storage and conversion,[15–17] sensing[18,19] and nanoelectronics devices.[14,20–22]

In recent years, a large subgroup of 2D crystals has attracted attention consisting of 2D conjugated polymer, which can be stabilized as monolayers by taking advantage of the chemistry of C and N. The strong C bonds give rise to the unique properties of graphene, while the ability of N to take many different positions enhances the option to form a strong covalent organic framework.[23,23–33] A monolayer of C_3N was recently successfully synthesized.[34] Due to its uniqe properties[35] several applications have been suggested including solar cell devices, electrolyte gating and doping of transistors, and anode material.[36–38] Monolayer C_3N is an indirect band-gap semiconductor and its electronic structure has been computed[34,39,40] by DFT calculations. An important issue is to make the intrinsic band gap of C_3N tunable, in order to extend its properties. Previously, it was shown that the properties of C_3N can be

View Article Online
DOI: 10.1039/C9CP03853A

tuned by adsorption of adatoms and doping,[5,41–46] adsorptions of molecules,[29,47,48] defect as well as strain engineering[5,46,47,49?,50] and other methods[51–53] The substitution of atoms into carbon nitride materials is of fundamental importance, enabling a wide range of applications by tailoring the electronic and magnetic properties.[54–56]

Using first-principles calculations, we carried out a detailed investigation of how various point defects including vacancies (single and double vacancy), Stone-Wales (SW) and anti-site defects affect the structure of C_3N and its electronic and magnetic properties. We demonstrate the capability of defect engineering to alter the properties of C_3N from nonmagnetic semiconductor to a metal and/or a magnetic ground state. Furthermore, we present a detailed study of the effect of substitution of H, O, S, F, Cl, B, C, N, Si, P, Li, Na, K, Be, Mg, Ca and Al atoms on the electronic and magnetic properties of C_3N. We analyze the modification of the band structure of C_3N as the underlying mechanism for the changes in its properties. One of the goals is to show how introducing the above impurities turns the semiconductor of C_3N into a metal, half-metal, spin-glass semiconductor or dilute-magnetic semiconductor. The effects of charging and strain on the substituted-C_3N are studied and we show how the band gap and magnetism can be modulated. The important point here is that a wide variety of electronic and magnetic properties, differing from pristine C_3N, emerge using the above methods.

Method

In this paper, we performed calculations of the electronic structure with geometric optimization, using spin-polarized density functional theory (DFT) as implemented in OpenMX Package.[57] This code self-consistently finds the eigenvalues and eigenfunctions of the Kohn-Sham equations for the systems under study using norm-conserving pseudopotentials,[58] and pseudoatomic orbitals (PAOs).[59,60] In addition, we used the Perdew-Burke-Ernzerhof generalized gradient approximation (GGA) for the exchange and correlation.[61] The K-points for

View Article Online
DOI: 10.1039/C9CP03853A

sampling over the Brillouin zone (BZ) were generated using the Monkhorst-Pack scheme.[62] With a k-mesh grid of $23 \times 23 \times 1$ for the primitive unit cell and scaled according to the size of the supercell. After convergence tests, we choose an energy cutoff 300 Ry so that the total-energy was converged with an accuracy below 1.0 meV/atom. The geometries were fully relaxed until the force acting on each atom was less than 1 meV/Å and we choose a large vacuum layer of 20 Å to avoid interaction between adjacent layers. The charge transfer was calculated using the Mulliken charge analysis.[63] In order to accurately describe the van der Waals (vdW) interaction in C_3N, we adopted the empirical correction method presented by Grimme (DFT-D2),[64] which has been proven reliable for describing the long-range vdW interactions. Simulated scanning tunneling microscopy (STM) images were obtained using the Tersoff-Hamann theory,[65] as supplied in the OpenMX code with a bias of 2.0 V and were graphed using WSxM software.[66]

Pristine C_3N

The atomic structure of C_3N is a planar hexagonal lattice, shown in Fig. 1(a). The lattice constant of C_3N is 4.861 Å, which agrees well with the experimental value of 4.75 Å[34] with bond lengths of 1.404 and 1.403 Å which are in good agreement with previous theoretical studies.[39,41,42,67] The difference charge density shows a high charge density around the N atoms, indicating charge transfer from C to N atoms. In order to provide visible guidance for experimental observations, first-principles DFT calculations were performed to calculate the STM image which is shown in Fig. 1(b). To produce the calculated STM image, the Kohn-Sham charge density was integrated at a voltage of +2.0 V. The atoms around C-N bonds are shows as bright spots. To correlate the STM image with the corresponding atomistic structure, we overlayered it with the C_3N lattice structure with the C (gray ball) and the N (blue ball) atoms. The orbital-projected electronic band structure of C_3N with corresponding DOS and PDOS, are shown in Figs. 1(c,d). Notice the valence band maximum

View Article Online
DOI: 10.1039/C9CP03853A

(VBM) of C_3N is dominated by N-p_z orbitals and the Dirac-cone at the k=point below E_F is formed by C-p_z orbitals. Our DFT calculations show that C_3N is an indirect semiconductor with 0.4 eV band gap which is in agreement with previous results.[41,42,67] The valence band maximum (VBM) and the conduction band minimum (CBM) are located between the Γ and **M** points. The DOS and PDOS are shown in Fig. 1(d). Since in C_3N two C atoms are replaced by N, the p_z orbital band is fully occupied by additional two electrons, leading to a semiconducting behavior. From PDOS, we see that the VBM is built up by N-p_z orbitals, whereas the CBM is dominated by C-p_z orbitals.

Topological defects

Recently, many methods including defect engineering,[53,68] applying electric field,[26] strain,[69,70] edge state[26,71] and heterostructuring[54,55] was used to change the properties of the carbon nitride materials. We investigate different topological defects in monolayer C_3N and in addition vacancies, Stone-Wales and anti-site defects. In order to investigate vacancies, we removed C and N atoms to produce single vacancy of the C atom SV_C or N atom SV_N, while for double vacancies, we remove C+C (DV_{CC}), N+N (DV_{NN}) and N+C (DV_{NC}) atoms respectively. For the Stone-Wales (SW) defect, we rotate a single C-C (SW_{CC}) or N-C (SW_{NC}) bond in C_3N by 90°, resulting in a structure with a pair of seven-membered and five-membered rings, respectively. For the anti-site defects, we replaced N with C atoms (i.e., exchanged the position of N and C atoms) (AS_{NC}). Typical defects are schematically shown in Fig. 2. With fully structural optimization, where all atoms are relaxed in all directions and calculations are performed using $2 \times 2 \times 1$ supercell of C_3N which contains 32 atoms (24 C and 8 N atoms).

In Fig. 3, we present the optimized structures with corresponding bond lengths and bond angles of SV_C and SV_N. The C and N atoms around the vacancy in C_3N undergo a Jahn-Teller distortion[72] and C and N atoms close to the vacancy site move towards each other to

View Article Online
DOI: 10.1039/C9CP03853A

form C-C or C-N bonds. For the reconstructed SV_C (SV_N), two C atoms bond together to build a joint pentagonal and nonagonal (i.e., the 5-9 configurations). Two C atoms around the vacancy are approaching each other, so the C-C (N-C) bond lengths are changed to 1.597 (1.730) and 1.550 (1.560) Å, respectively, which differs from pristine C_3N (1.403 and 1.404 Å) (see Fig. 3). For SV_C, upon structural optimization the same symmetry and a planar structure of C_3N is found. In DV_{CC} case, we observed no deviation from the planar configuration upon structural relaxation and it exhibits a non-reconstructed structure, while DV_{NC} shows reconstructed structure and two C atoms bond together to build two pentagon and one heptagon (i.e. the 5-8-5 configurations) (see Fig. 3). The distance between dangling bonds in DV_{CC} is found to be about 1.404 Å and the bond lengths of C and N atoms around the vacancies become 2.041 and 1.404 Å. The bond lengths of DV_{NC} are 1.404 and 1.404 Å (see Fig. 3). The DV_{NN} shows a non-reconstructed structure and the bond lengths of C and N atoms around the vacancies become 1.44 and 1.43 Å. For AS_{NC} we see a negligible bond length elongation in the modified structure. The C-C bond length undergoes a small modification from 1.404 to 1.406 Å, and the N-C bond length is calculated to be 1.400 Å. As can be seen from Fig. 3, after the formation of SW defect, four neighboring hexagons of C_3N are transformed into one pentagon and two heptagons (the 55-77 configurations), and C_3N maintains its planer 2D structure. Through 90° rotation of a dimer, the C-C bond becomes stronger than the one in pristine C_3N, and its length decreases from 2.281 to 2.191 Å. Due to the shortening of bond lengths along the direction parallel to the pentagons, the lattice constant decreases from 23.212 to 23.041 Å.

The effect of SV defects on the electronic and magnetic properties of C_3N, are shown in Fig. 4. It is noticeable that the band structure of pristine C_3N is strongly disturbed by the vacancy defects. The SV_C and SV_N turns pristine C_3N into a metal and ferromagnetic-metal, respectively. In addition, SV_N has 0.3 μ_B magnetic moment due to the dangling bond around the defect sites with an unpaired electron. For DV_{CC} and DV_{NC}, similar to what we have for the SV-defect, states appear near E_F, resulting in metallic characteristics in

View Article Online
DOI: 10.1039/C9CP03853A

the electronic structure. Our results show that DV_{NN}, becomes a ferromagnetic-metal and induces 3.5 μ_B magnetic moment to C_3N. We see that AS_{NC}, is a semiconductor with 0.2 eV indirect band gap. After introducing the SW defects, the electronic states experience a shift due to the breaking of the hexagonal lattice symmetry by the SW defect. The SW-C_3N, is an indirect semiconductor with 0.2 eV band gap due to the introduction of an energy level near the CB, which is related to some bonds of both C and N atoms around the defect. The VBM (CBM) is located at Γ (between M and Γ points). Moreover, the band becomes flatter which indicates a strongly localized charge around these defects.

It is also evident from the DOS and PDOS in the same panel, that the state at E_F of SV-C_3N belongs to the C/N-p_z orbital around the missing atom which confirms the metallic behavior of SV-C_3N. By analyzing of PDOS it is clear that the magnetism in SV_N are derived from the C-p orbitals of the C atoms in SV_N. For the case of DV_{CC}, we found that the state at E_F belongs to the s and p-orbitals of C and N atoms locating around the missing atom which confirms the metallic behavior, whereas, for DV_{NC}, the state around E_F originates from C/N-p_z orbitals. While the VB and CB of DV_{NN} belongs to the C/N-s,$p_{x,y}$ orbital, the VB and CB of AS_{NC} belongs to the C/N-p_z orbitals. The VB of SW_{CC} and SW_{NC} has N-p_z orbital and the CB is build up of the C-p_z orbital around the defect, which results in semiconducting behavior. To provide visible guidance for experiments, the simulated STM images of different defects, are shown in Fig. S1 (see supplementary information (SI)), where the bright and dark spots have been used for a more succinct demonstration. Difference spin density for SV_N and DV_{NN} are shown in Fig. 5 in the insets. The blue and yellow regions represent the ↑ and ↓ spin states, respectively. Notice that it is symmetrical and localized around the defect which is a consequence of the centrosymmetric structure of SV_N.

View Article Online
DOI: 10.1039/C9CP03853A

Atom substitution

To further shed light on the underlying mechanism of the electronic and magnetic properties, we investigate the spin-polarized band structures of atoms substituted in C_3N. Recently, adsorption and substitution of atoms[73–77] and surface functionalizing with molecules[78,79] of C_2N was studied. We found that the band structure of pristine C_3N was strongly disturbed when atoms are substituted, thus the bonding between these atoms and the C_3N lattice should be covalent. With fully structural optimization, where all atoms are relaxed in all directions and calculations are performed using $2 \times 2 \times 1$ supercell of C_3N which contains 32 atoms (24 C and 8 N atoms).

We consider two substitution sites: (1) the C host atom site (Sb_C) and (2) the N host atom site (Sb_N). The change of lattice constant is shown in Fig. 6(a) and a schematic view of two substitution sites are shown in the inset. The substitution of foreign atoms with C (N) host atom of C_3N, is labeled as Sb_C-C_3N (Sb_N-C_3N). For instance, substitution of H atom for C (N), is labeled as H_C-C_3N (H_N-C_3N). The induced strain to the lattice structure of the C_3N can be estimated by calculating $(a\text{-}a_0)/a_0$, where a_0 is the lattice constant of pristine C_3N and a is the lattice constant of Sb-C_3N. The induced strain is plotted in Figs. 6(b,c). Lattice deformation of the substituted-C_3N structure exhibit an increase of induced distortion to the C_3N lattice constant. From Figs. 6(b,c), we find that the strain for H, O, S, F, Cl, B, Si and P substitution for C and N sites varies between 0.5 to 5 %. For the Li, Na, K, Be, Mg, Ca and Al atoms the strain varies between 2.5 to 9 % which is significantly larger. Notice the increase in lattice constant with the atomic number which is present in both cases (see Fig. 6(a)). The energy band gap and magnetic moment for different species of atoms are shown in Figs. 6(d,e) and Figs. 6(f,g), respectively.

The interaction between the substituted atoms and the C_3N lattice can induce a charge redistribution. The Mulliken population analysis was performed to quantitatively analyze this effect. Positive (negative) charge transfer indicates a loss (gain) of electrons for each substituted atom to (from) C_3N. In pristine C_3N there is a charge transfer from C to N

View Article Online
DOI: 10.1039/C9CP03853A

atoms. However, those C and N atoms in the substituted C_3N, have different Mulliken charges because of the different arrangement of atoms. The redistribution of charge for substituted C_3N depends mainly on the incorporation of substituted atom into the C and N lattice. For example, substitution of C host atom with Li and P atoms, induce Mulliken charges of -0.48 e and +0.53 e, respectively, while substitution with Na and Al yield +0.14 e and +0.23 e, respectively. The C and N atoms bonded to the substitutional atoms have much larger Mulliken charges than those in pristine C_3N. This difference can be attributed to the different atomic radius, electro-negativities, and their bond length of C and N atom with the foreign atoms.

The optimized structures of H, O, S, F, Cl, B, C, Si, N and P substituted C_3N on C or N sites with their corresponding structural parameters including atomic bond length and angles are shown in Figs. 7(a,b). In the case of reconstruction, the honeycomb structure is deformed locally and the host atoms are pushed away from its lattice position. It can be seen that for H_C and H_N, the H atom becomes bonded to the neighboring C atom and the resulting length of the H-C bond is 1.116 and 1.086 Å, respectively. The O and F atoms interact through sp^2-hybridization, resulting in the formation of two and three σ bonds with the neighboring C atoms of C_3N, respectively. The bond length of O_C, O_N are 1.341 and 1.541 Å, and the C-O-C bond angles are 135° and 119°, respectively. For F_C and F_N, the F-C bond length is 1.582 and 1.712 Å, and the C-F-C bond angle is 145° and 119°, respectively. We can see a strong effect on the planar structure of C_3N for F_C. For B_C and B_N, the B atoms form one and three σ bonds with the neighboring N and C atoms, respectively. and the bond length with the nearest N atom is 1.441 Å, while for B_N the bond length with the nearest C atoms is 1.482 Å and the C-B-C bond angle is 120°, with a small in plane distortion of the C_3N lattice. The Si and P atomic radius is larger than that of C or N atom and as a consequence the Si and P atoms induce a structural deformation along the direction of the C_3N plane, leading to an expansion of the lattice parameter with $\sim 3.0\%$. The change in bond lengths and angles reflect the size of substituted atoms, and due to

View Article Online
DOI: 10.1039/C9CP03853A

changes in the optimized structure the charge transfer between the substituted atoms and the substrate are modified. The structural parameters for these atomic structures are given in the supplementary information (SI).

The electronic structure of H, O, S, F, Cl, B, C, Si, N and P atoms substituted C_3N, are shown in Figs. 8(a,b). The blue-lines and red-dash lines represent up and down spin states, respectively. The electronic states of C_3N after substitution of different atoms are listed in Table1. The corresponding electronic states are specified as metal (M), half-metal (HM), ferromagnetic-metal (FM), spin-glass semiconductor (SG-SC), dilute-magnetic semiconductor (DM-SC) and semiconductor (SC) and are listed in Table I. The band gap and magnetic moment are indicated inside parentheses. In comparison with pristine C_3N, the shape of the electronic structure of Sb-C_3N is significantly modified. The H_C, Cl_C, H_N, O_N and S_N are metal, while O_C is a semiconductor with 0.6 eV direct band gap, where the VBM and CBM are located at the Γ point. We can see that S_C and Cl_N are indirect semiconductors with band gap of 0.33 eV and the VBM and CBM are located at the K point and between the M and Γ point, respectively. Moreover, S_C exhibit a p-type semiconductor, because these atoms gain electrons, resulting in a down shift of the E_F inside the VB edge. F_C is a dilute-magnetic semiconductor and the excess electron of the substituted F atom relative to C leads to spin-polarization and induces a magnetic moment of 1 μ_B in the ground state per F atom. B_C is a metal, while B_N is an indirect semiconductor with 0.5 eV band gap. Notice that the N atom has two extra electrons on the outer shell as compared to B which influences the VB and CB of C_3N. These excess electrons of the substituted N atom leads to a filling of the VB edge, similar to a p-type semiconductor and as a result B_N exhibit hole doping and thus causes a down shift of E_F. Also Si_C is a direct semiconductor with 0.34 eV band gap, while Si_N becomes a metal and the impurity states appear near the VB and CB edge.

The electronic structure of H, O, S, F, Cl, B, C, Si, N and P atoms substituted C_3N, are shown in Figs. 9(a,b). We found no spin polarized band structure for N_C, P_C, C_N, Si_N

View Article Online
DOI: 10.1039/C9CP03853A

and P_N which exhibit metallic characteristics with their E_F crossing the electronic states. For Cl_C the electron states near E_F are mainly governed by the C/N-p_z orbitals and for Cl_N are governed by the C-$p_{x,y}$, N-p_z and Cl-s orbitals. We found that the VBM of Cl_C is due to the hybridization of Cl-s with C-$p_{x,y}$ and N-p_z orbitals of the nearest atoms and CBM of Cl_C originates from Cl-$p_{x,y}$ with $p_{x,y}$ orbitals of the nearest C atoms. The VBM of S_C is due to the hybridization of S-$s, p_{x,y}$ with $p_{x,y}$ orbitals of the nearest N atoms and the CBM of S_CN originates from S-p_z with p_z orbitals of the nearest C atoms. For F_C there is an asymmetric spin splitting around E_F and as a consequence the defected structure becomes a dilute-magnetic semiconductor with an induced magnetic moment.

The discussion of corresponding PDOS further reveals that these asymmetric impurity states in the band gap mainly originates from the hybridization of N/F-2p and the C-2p orbitals leading to a magnetic moment of 1 μ_B. However for F_N, the hybridization is slightly different and the state near E_F mainly originates from the F-3s and C-p_z orbital states. PDOS of B_C shows that the CBM arises from the B-p_z and C/N-p_z orbitals. Also hybridization between the B-p_z and C/N-p_z orbitals mainly contributes to the VBM. For Si_C, Si being in the same group as C in the periodic table with a larger atomic radius, distorts the planar structure of C_3N and causes an increase in the bond length. VBM of C_3N is not influenced much upon substitution, where the states originate from Si-p_z orbitals. DOS and PDOS of P_C and P_N, show that both the CBM and VBM are composed of P-p_z and C-p_z orbitals. As expected, DOS of the B_C, N_C, P_C, B_C, C_N and Si_N, shows that the interaction between these atoms and C or N host atoms is responsible for the semiconductor to metal transition. Based on the calculated PDOS, both the CBM and VBM receive mainly contributions from the hybridization of the p_z orbitals.

The optimized atomic structures of Li, Na, K, Be, Mg, Ca and Al substituted C_3N and corresponding structural parameters including atomic bond length and bond angles, are shown in Fig. S2. Figs. 10(a,b) show the electronic band structure of Li, Na, K, Be, Mg, Ca and Al substitution in C_3N, while Na_C is ferromagnetic-metal with 1.3 μ_B magnetic

View Article Online
DOI: 10.1039/C9CP03853A

moment. Interestingly, Na_N and K_N, exhibit spin-glass semiconductor behavior with 1.9 and 2 μ_B magnetic moments, respectively. Namely, the $\uparrow$ spin channel is gapless, while the $\downarrow$ spin channel is a semiconductor and the VBM touches the Fermi level. Such spin-gapless semiconductors are of particular interest for e.g. spin photo-diodes, spin detectors and electromagnetic radiation generators for a wide range of wavelengths based on spin photo-conductivity. We found that Be_C, Mg_C, Li_N, Li_C, K_C and Be_N, are metallic, while Ca_C and Mg_N are ferromagnetic-metals with induced 1.3 and 0.7 μ_B magnetic moments, respectively. Al_N is a direct semiconductor with 0.43 eV band gap where the VBM and CBM are located at the Γ point. Unlike Ca_C, we see that Ca_N remains a direct semiconductor with a 1.0 eV band gap in the $\downarrow$ spin channel, whereas the $\uparrow$ spin channel is metallic, thus Ca_N is a half-metal with 1 μ_B magnetic moment. This suggests that the charge carriers within the energy bands in the vicinity of E_F are mobile, which is not only useful for electrical conduction but also for magnetic coupling. Notice that the half-metallic behavior of Ca_N can be useful in spintronics. Finally, Al_N is a direct semiconductor with band gap of 0.43 eV, while VBM and CBM are located at the Γ point. DOS and PDOS of Li, Na, K, Be, Mg, Ca and Al substituted C_3N, are shown in Fig. S3. Simulated STM images of C_3N substituted with Si, Na and Mg atoms, are plotted in Fig. S4.

Charging and strain effects

Now, we continue our exploration by considering the effects of charging and strain where we will limit ourselves to the investigation of Na_C and Na_N systems. A good starting point is to calculate the change of the magnetic moment with charging where we consider the case q = +1 e (when one electron is removed) and q = -1 e (when one electron is added). The corresponding electronic band structures are shown in Figs. 11(a,b) Our results show that Na_C-C_3N and Na_N-C_3N are ferromagnetic-metal and spin-glass semiconductor, which have 0.3 and 1.9 μ_B magnetic moments without charging. We see that the magnetic moment of

View Article Online
DOI: 10.1039/C9CP03853A

Na_C-C_3N increases to 0.48 μ_B for q = +1 e and preserve the ferromagnetic metal character. Whereas for the excess electronic charge of q = -1 e, the magnetic moment decreases to zero and it becomes a nonmagnetic semiconductor. In the case of Na_N-C_3N, the magnetic moment reaches 2.2 μ_B when 1 electron is removed (q = +1 e) and it transforms to a ferromagnetic-metal. Under excess electronic charge (q = -1 e), the reverse situation is predicted where the magnetic moment decreases to 0.95 μ_B.

The tensile and compressive strain are defined as $\varepsilon = (\frac{a \pm a_0}{a_0}) \times 100$, where a and a_0 are strained and non-strained lattice constants, respectively. The positive and negative values denotes tensile and compression states, respectively. Uniaxial strain is applied along zigzag directions and the atomic positions are optimized. Figs. 11(c-f) show the DOS of Na_C and Na_N for a strain of ε (ε= -8, -6, -4, -2, 0, +2, +4, +6 and +8 %). We see that the magnetic moment arises from orbital states near E_F, whose spin degeneracy is lifted by strain. The electronic structure of Na substituted on C_3N as a function of uniaxial strain are shown in Figs. 12(a,b) . The band structure changes with ε in $\uparrow$ and $\downarrow$ spin channels and the magnetic moment decreases with ε for tensile (from +2 to +8 %) and compression (from -2 to -8 %) strains. The magnetic moment as a function of uniaxial strain (tensile and compression), are shown in Fig. 13. Whereas for Na_N, which is different with Na_C and we can see that the magnetic moment decreases for tensile (from +2 to +8 %), while increases for compression strain (from -2 to -8 %). Moreover, both tensile and compression states changes the magnetic moment of Na_C and Na_N almost linearly with strain The magnetic moment changes with respect to ε and more rapidly when compressing the Na_C- and $Na_N - C_3N$.

Conclusion and Summary

In summary by using first-principle calculations within the framework of DFT, a systematic investigation of the effect of topological defects including single and double vacancies, Stone-Wales and anti-site, on the structure and electronic properties of C_3N was presented. Our

View Article Online
DOI: 10.1039/C9CP03853A

results show that for both single and double vacancies C_3N becomes a metal, except in the case of a single vacancy of N and double vacancy of N+N. C_3N with anti-site defects when C_3N becomes a direct semiconductor with 0.2 eV band gap. With Stone-Wales defects, C_3N becomes an indirect semiconductor with the band gap of 0.2 eV. Furthermore, we studied the effects due to H, O, S, F, Cl, B, C, N, Si, P, Li, Na, K, Be, Mg, Ca and Al substitution on the electronic properties of C_3N. When the C site is substituted with O, S and Si atoms, the system remains a semiconductor with band gap in the range of 0.25-0.75 eV, while with H, Cl, B, P, Li, Na, K, Be and Mg atoms the system turns into a metal. Also, upon substitution of the native C with F atom, C_3N becomes a dilute-magnetic semiconductor, while with Ca substitution it is a ferromagnetic-metal. Moreover, when N is replaced with H, O, S, C, Si, P, Li and Be atoms the system turns into a metal and with F, Cl, B and Al atoms becomes a semiconductor. With Mg and Ca atoms it becomes a ferromagnetic-metal and half-metal with induces magnetic moments of 0.3 μ_B and 2 μ_B, respectively. In addition, with Na and K shows spin-glass semiconductor. Moreover, we investigated the effect of charging and strain on the electronic structure of C_3N, in which native C and N atoms are substituted with Na atom. Our result shows that the magnetic moment with applied charging and strain can be tuned. It is possible to tune the magnetism by controlling the Fermi level via external fields such as by charging and strain. Our calculations predict that the introduction of typical topological defects or by substitution of atoms in C_3N, provides an interesting way to tune the electronic and magnetic properties which can be useful in a diversity of applications including solar cells, sensors, nanoelectronics, optoelectronics and spintronic devices.

Acknowledgment

This work was supported by the Flemish Science Foundation (FW0-Vl).

View Article Online
DOI: 10.1039/C9CP03853A

References

(1) Novoselov, K. S.; Geim, A. K.; Morozov, S. V.; Jiang, D.; Zhang, Y.; Dubonos, S. V.; Grigorieva, I. V.; Firsov, A. A. Electric Field Effect in Atomically Thin Carbon Films. *Science* **2004**, *306*, 666–669.

(2) Chan, K. T.; Neaton, J. B.; Cohen, M. L. First-Principles Study of Metal Adatom Adsorption on Graphene. *Phys. Rev. B* **2008**, *77*, 235430.

(3) Sahin, H.; Peeters, F. M. Adsorption of Alkali, Alkaline-Earth, and 3*d* Transition Metal Atoms on Silicene. *Phys. Rev. B* **2013**, *87*, 085423.

(4) Pang, Q.; Li, L.; Zhang, L.-L.; Zhang, C.; Song, Y.-L. Functionalization of Germanene by Metal Atoms Adsorption: A First-Principles Study. *Can. J. Phys.* **2015**, *93*, 1310–1318.

(5) Bafekry, A.; Farjami Shayesteh, S.; Peeters, F. M. C_3N Monolayer: Exploring the Emerging of Novel Electronic and Magnetic Properties with Adatom Adsorption, Functionalizations, Electric field, Charging and Strain. *J. Phys. Chem. C.* **2019**, *123*, 12485–12499.

(6) A. Bafekry, S. F. S., M. Ghergherehchi; Peeters, F. Adsorption of molecules on C_3N nanosheet: A first-principles calculations. *Chem. Phys.* **2019**, *526*, 110442.

(7) Kadioglu, Y.; Ersan, F.; GÃűkoÄ§lu, G.; ÃIJzengi AktÃijrk, O.; AktÃijrk, E. Adsorption of Alkali and Alkaline-Earth Metal Atoms on Stanene: A First-Principles Study. *Mater. Chem. Phys.* **2016**, *180*, 326–331.

(8) Li, Y.; Xia, C.; Du, J.; Xiong, W.; Li, X.; Wei, S. Influences of the Adsorption of Different Elements on the Electronic Structures of a Tin Sulfide Monolayer. *Phys. Chem. Chem. Phys.* **2017**, *19*, 5423–5429.

View Article Online
DOI: 10.1039/C9CP03853A

(9) Lalitha, M.; Mahadevan, S. S.; Lakshmipathi, S. Improved Lithium Adsorption in Boron- and Nitrogen-Substituted Graphene Derivatives. *J. Mater. Sci.* **2017**, *52*, 815–831.

(10) Bafekry, A.; Ghergherehchi, M.; Farjami Shayesteh, S. Tuning the electronic and magnetic properties of antimonene nanosheets via point defects and external fields: first-principles calculations. *Phys. Chem. Chem. Phys.* **2019**, *21*, 10552–10566.

(11) Wang, X.; Jiang, X.; Sharman, E.; Yang, L.; Li, X.; Zhang, G.; Zhao, J.; Luo, Y.; Jiang, J. Isolating Hydrogen from Oxygen in Photocatalytic Water Splitting with a Carbon-Quantum-dot/carbon-Nitride Hybrid. *J. Mater. Chem. A* **2019**, *7*, 6143–6148.

(12) Sun, M.; Wang, S.; Du, Y.; Yu, J.; Tang, W. Transition Metal Doped Arsenene: A First-Principles Study. *Appl. Surf. Sci.* **2016**, *389*, 594 – 600.

(13) Sun, M.; Ren, Q.; Wang, S.; Zhang, Y.; Du, Y.; Yu, J.; Tang, W. Magnetism in Transition-Metal-Doped Germanene: A First-Principles Study. *Comput. Mater. Sci.* **2016**, *118*, 112 – 116.

(14) Cheng, Y. C.; Zhu, Z. Y.; Mi, W. B.; Guo, Z. B.; Schwingenschlögl, U. Prediction of Two-Dimensional Diluted Magnetic Semiconductors: Doped Monolayer MoS_2 Systems. *Phys. Rev. B* **2013**, *87*, 100401.

(15) ÃIJzengi AktÃijrk, O.; Tomak, M. Lithium and Antimony Adsorbed on Graphene Studied by First-Principles Calculations. *Appl. Surf. Sci.* **2011**, *258*, 800 – 805.

(16) Gao, S.; Ren, Z.; Wan, L.; Zheng, J.; Guo, P.; Zhou, Y. Density Functional Theory Prediction for Diffusion of Lithium on Boron-Doped Graphene Surface. *Appl. Surf. Sci.* **2011**, *257*, 7443 – 7446.

(17) Roy-Mayhew, J. D.; Bozym, D. J.; Punckt, C.; Aksay, I. A. Functionalized Graphene

View Article Online
DOI: 10.1039/C9CP03853A

as a Catalytic Counter Electrode in Dye-Sensitized Solar Cells. *ACS Nano* **2010**, *4*, 6203–6211.

(18) Ganji, M. D.; Sharifi, N.; Ardjmand, M.; Ahangari, M. G. Pt-Decorated Graphene as Superior Media for H_2S Adsorption: A First-Principles Study. *Appl. Surf. Sci.* **2012**, *261*, 697 – 704.

(19) Lee, Y.; Lee, S.; Hwang, Y.; Chung, Y.-C. Modulating Magnetic Characteristics of Pt Embedded Graphene by Gas Adsorption (N_2, O_2, NO_2, SO_2). *Appl. Surf. Sci.* **2014**, *289*, 445 – 449.

(20) Khan, I.; Hong, J. Manipulation of Magnetic State in Phosphorene Layer by Non-Magnetic Impurity Doping. *New J. Phys.* **2015**, *17*, 023056.

(21) Seixas, L.; Carvalho, A.; Castro Neto, A. H. Atomically Thin Dilute Magnetism in Co-Doped Phosphorene. *Phys. Rev. B* **2015**, *91*, 155138.

(22) Ramasubramaniam, A.; Naveh, D. Mn-Doped Monolayer MoS_2: An Atomically Thin Dilute Magnetic Semiconductor. *Phys. Rev. B* **2013**, *87*, 195201.

(23) SARIKURT, S.; ERSAN, F. Phononic Stability Analysis of Two-Dimensional Carbon Nitride Monolayers. *Marmara Fen Bilimleri Dergisi* **2018**, *30*, 383 – 387.

(24) Shirazi, A.; Abadi, R.; Izadifar, M.; Alajlan, N.; Rabczuk, T. Mechanical Responses of Rristine and Defective C_3N Nanosheets Studied by Molecular Dynamics Simulations. *Comput. Mater. Sci.* **2018**, *147*, 316 – 321.

(25) Shi, L.-B.; Zhang, Y.-Y.; Xiu, X.-M.; Dong, H.-K. Structural Characteristics and Strain Behavior of Two-Dimensional C_3NÂĂ: First Principles Calculations. *Carbon* **2018**, *134*, 103 – 111.

(26) Wang, D.; Bao, Y.; Wu, T.; Gan, S.; Han, D.; Niu, L. First-Principles Study of the Role of Strain and Hydrogenation on C_3N. *Carbon* **2018**, *134*, 22 – 28.

View Article Online
DOI: 10.1039/C9CP03853A

(27) Zhou, X.; Feng, W.; Guan, S.; Fu, B.; Su, W.; Yao, Y. Computational characterization of monolayer C_3N: A two-dimensional nitrogen-graphene crystal. *J. Mater. Research* **2017**, *32*, 2993âĂŞ3001.

(28) Zhou, Y.; Gao, G.; Kang, J.; Chu, W.; Wang, L.-W. Transition metal-embedded two-dimensional C_3N as a highly active electrocatalyst for oxygen evolution and reduction reactions. *J. Mater. Chem. A* **2019**, *7*, 12050–12059.

(29) Esrafili, M. D.; Heydari, S. B-doped C_3N monolayer: a robust catalyst for oxidation of carbon monoxide. *Theoretical Chemistry Accounts* **2019**, *138*, 57.

(30) Esrafili, M. D.; Heydari, S. An effective approach for tuning catalytic activity of C_3N nanosheets: Chemical-doping with the Si atom. *J. Molecular Graphics and Modelling* **2019**, *92*, 320 – 328.

(31) Abdullahi, Y. Z.; Yoon, T. L.; Halim, M. M.; Hashim, M. R.; Lim, T. L. Mechanical and electronic properties of graphitic carbon nitride sheet: First-principles calculations. *Solid State Communications* **2016**, *248*, 144 – 150.

(32) Mortazavi, B.; Shahrokhi, M.; Raeisi, M.; Zhuang, X.; Pereira, L. F. C.; Rabczuk, T. Outstanding strength, optical characteristics and thermal conductivity of graphene-like BC_3 and BC_6N semiconductors. *Carbon* **2019**, *149*, 733 – 742.

(33) Mortazavi, B.; Shahrokhi, M.; Shapeev, A. V.; Rabczuk, T.; Zhuang, X. Prediction of C_7N_6 and C_9N_4: stable and strong porous carbon-nitride nanosheets with attractive electronic and optical properties. *J. Mater. Chem. C* **2019**, –.

(34) Mahmood, J.; Lee, E. K.; Jung, M.; Shin, D.; Choi, H.-J.; Seo, J.-M.; Jung, S.-M.; Kim, D.; Li, F.; Lah, M. S.; Park, N.; Shin, H.-J.; Oh, J. H.; Baek, J.-B. Two-Dimensional Polyaniline (C_3N) from Carbonized Organic Single Crystals in Solid State. *Proceedings of the National Academy of Sciences* **2016**, *113*, 7414–7419.

View Article Online
DOI: 10.1039/C9CP03853A

(35) Hong, Y.; Zhang, J.; Zeng, X. C. Monolayer and bilayer polyaniline C_3N: two-dimensional semiconductors with high thermal conductivity. *Nanoscale* **2018**, *10*, 4301–4310.

(36) Chang, M.-Y.; Wu, C.-S.; Chen, Y.-F.; Hsieh, B.-Z.; Huang, W.-Y.; Ho, K.-S.; Hsieh, T.-H.; Han, Y.-K. Polymer Solar Cells Incorporating One-Dimensional Polyaniline Nanotubes. *Organic Electronic.* **2008**, *9*, 1136 – 1139.

(37) Alam, M. M.; Wang, J.; Guo, Y.; Lee, S. P.; Tseng, H.-R. Electrolyte-Gated Transistors Based on Conducting Polymer Nanowire Junction Arrays. *J. Phys. Chem. B* **2005**, *109*, 12777–12784.

(38) Jiantie, X.; Javeed, M.; Yuhai, D.; Shixue, D.; Feng, L.; Liming, D.; Beom, B. J. 2D Frameworks of C_2N and C_3N as New Anode Materials for LithiumâĂŘIon Batteries. *Adv. Mater. 29*, 1702007.

(39) Mizuno, S.; Fujita, M.; Nakao, K. Electronic States of Graphitic Heterocompounds of Carbon, Boron and Nitrogen. *Synthetic Metals* **1995**, *71*, 1869 – 1870.

(40) Qianku, H.; Qinghua, W.; Haiyan, W.; Julong, H.; Guanglei, Z. FirstâĂŘ-Principles Studies of Structural and Electronic Properties of Layered C_3N Phases. *physica status solidi (b)* **2011**, *249*, 784–788.

(41) Makaremi, M.; Mortazavi, B.; Singh, C. V. Adsorption of Metallic, Metalloidic, and Nonmetallic Adatoms on Two-Dimensional C_3N. *J. Phys. Chem. C.* **2017**, *121*, 18575 – 18583.

(42) Pashangpour, M.; Peyghan, A. A. Adsorption of Carbon Monoxide on the Pristine, B- and Al-Doped C_3N Nanosheets. *J. Molecular Model.* **2015**, *21*, 116.

(43) Tagani, M. B. Electrical and Mechanical Properties of a Fully Hydrogenated Two-Dimensional Polyaniline Sheet. *Comput. Mater. Sci.* **2018**, *153*, 126 – 133.

View Article Online
DOI: 10.1039/C9CP03853A

(44) Yang, B.; Fu, Z. Comparative Study of C_3N- and Graphene-Supported Single-Atom Pt. *J. Phys. Chem. C* **2019**, *123*, 5731–5735.

(45) He, B.; Shen, J.; Ma, D.; Lu, Z.; Yang, Z. Boron-Doped C_3N Monolayer as a Promising Metal-Free Oxygen Reduction Reaction Catalyst: A Theoretical Insight. *J. Phys. Chem. C* **2018**, *122*, 20312–20322.

(46) Xie, L.; Yang, L.; Ge, W.; Wang, X.; Jiang, J. Bandgap tuning of C_3N monolayer: A first-principles study. *Chem. Phys.* **2019**, *520*, 40 – 46.

(47) Ma, D.; Zhang, J.; Tang, Y.; Fu, Z.; Yang, Z.; Lu, Z. Repairing Single and Double Atomic Vacancies in a C_3N Monolayer with CO or NO Molecules: A First-Principles Study. *Phys. Chem. Chem. Phys.* **2018**, *20*, 13517–13527.

(48) Rani, S.; Ray, S. Detection of gas molecule using C_3N island single electron transistor. *Carbon* **2019**, *144*, 235 – 240.

(49) Guo, G.-C.; Wang, R.-Z.; Ming, B.-M.; Wang, C.; Luo, S.-W.; Lai, C.; Zhang, M. Trap Effects on Vacancy Defect of C_3N as Anode Material in Li-Ion Battery. *Appl. Surf. Sci.* **2019**, *475*, 102 – 108.

(50) Ren, Y.; Cheng, F.; Zhou, X.; Chang, K.; Zhou, G. Tunable Mechanical, Electronic and Magnetic Properties of Monolayer C_3N Nanoribbons by External Fields. *Carbon* **2019**, *143*, 14 – 20.

(51) Tagani, M. B.; Vishkayi, S. I. Polyaniline (C_3N) Nanoribbons: Magnetic Metal, Semiconductor, and Half-Metal. *J. Appl. Phys.* **2018**, *124*, 084304.

(52) Li, W.; Dai, X.; Morrone, J.; Zhang, G.; Zhou, R. Thickness Dependent Semiconductor-to-Metal Transition of Two-Dimensional Polyaniline with Unique Work Functions. *Nanoscale* **2017**, *9*, 12025–12031.

View Article Online
DOI: 10.1039/C9CP03853A

(53) Zhang, C.; Huang, H.; Ni, X.; Zhou, Y.; Kang, L.; Jiang, W.; Chen, H.; Zhong, J.; Liu, F. Band Gap Reduction in van der Waals layered 2D Materials via a De-Charge Transfer Mechanism. *Nanoscale* **2018**, *10*, 16759–16764.

(54) Zheng, Z.; Wang, X.; Mi, W. Tunable Electronic Structure in Stained Two Dimensional van der Waals g-C_2N/XSe_2 (X = Mo, W) Heterostructures. *Physica E: Low-dimensional Systems and Nanostructures* **2017**, *94*, 148 – 152.

(55) Kumar, R.; Das, D.; Singh, A. K. C_2N/WS_2 van der Waals type-II Heterostructure as a Promising Water Splitting Photocatalyst. *J. Catalysis* **2018**, *359*, 143 – 150.

(56) Kishore, M. A.; Sjastad, A. O.; Ravindran, P. Influence of Hydrogen and Halogen Adsorption on the Photocatalytic Water Splitting Activity of C_2N Monolayer: A First-Principles Study. *Carbon* **2019**, *141*, 50 – 58.

(57) Ozaki, T.; Nishio, K.; Kino, H. Efficient Implementation of the Nonequilibrium Green Function Method for Electronic Transport Calculations. *Phys. Rev. B* **2010**, *81*, 035116.

(58) Troullier, N.; Martins, J. L. Efficient Pseudopotentials for Plane-Wave Calculations. *Phys. Rev. B* **1991**, *43*, 1993–2006.

(59) Ozaki, T. Variationally Optimized Atomic Orbitals for Large-Scale Electronic Structures. *Phys. Rev. B* **2003**, *67*, 155108.

(60) Ozaki, T.; Kino, H. Numerical Atomic Basis Orbitals from H to Kr. *Phys. Rev. B* **2004**, *69*, 195113.

(61) Perdew, J. P.; Burke, K.; Ernzerhof, M. Generalized Gradient Approximation Made Simple. *Phys. Rev. Lett.* **1996**, *77*, 3865–3868.

(62) Monkhorst, H. J.; Pack, J. D. Special Points for Brillouin-Zone Integrations. *Phys. Rev. B* **1976**, *13*, 5188–5192.

View Article Online
DOI: 10.1039/C9CP03853A

(63) Mulliken, R. S. Electronic Population Analysis on LCAOâĂŘMO Molecular Wave Functions. IV. Bonding and Antibonding in LCAO and Valence Bond Theories. *J. Chem. Phys.* **1955**, *23*, 2343–2346.

(64) Bucko, T.; Hafner, J.; Lebegue, S.; Angyan, J. G. Improved Description of the Structure of Molecular and Layered Crystals: Ab Initio DFT Calculations with van der Waals Corrections. *J. Phys. Chem. A* **2010**, *114*, 11814–11824.

(65) Tersoff, J.; Hamann, D. R. Theory and Application for the Scanning Tunneling Microscope. *Phys. Rev. Lett.* **1983**, *50*, 1998–2001.

(66) Horcas, I.; Fernandez, R.; Gomez-Rodriguez, J. M.; Colchero, J.; GÃşomez-Herrero, J.; Baro, A. M. WSxM: A Software for Scanning Probe Microscopy and a Tool for Nanotechnology. *Rev. Sci. Inst.* **2007**, *78*, 013705.

(67) Mortazavi, B. Ultra High Stiffness and Thermal Conductivity of Graphene Like C_3N. *Carbon* **2017**, *118*, 25 – 34.

(68) Yagmurcukardes, M.; Horzum, S.; Torun, E.; Peeters, F. M.; Tugrul Senger, R. Nitrogenated, Phosphorated and Arsenicated Monolayer Holey Graphenes. *Phys. Chem. Chem. Phys.* **2016**, *18*, 3144–3150.

(69) Abdullahi, Y. Z.; Yoon, T. L.; Lim, T. L. Elastic and Electronic Properties of C_2N Monolayer: First-Principles Calculation. *Materials Research Express* **2019**, *6*, 025601.

(70) Guan, S.; Cheng, Y.; Liu, C.; Han, J.; Lu, Y.; Yang, S. A.; Yao, Y. Effects of Strain on Electronic and Optic Properties of Holey Two-Dimensional C_2N Crystals. *Appl. Phys. Lett.* **2015**, *107*, 231904.

(71) Yu, H.; Jiang, X.; Cai, M.; Feng, J.; Chen, X.; Yang, X.; Liu, Y. Electronic and Magnetic Properties of Zigzag C_2N-h2D Nanoribbons: Edge and Width Effects. *Chem. Phys. Lett.* **2017**, *685*, 363 – 370.

View Article Online
DOI: 10.1039/C9CP03853A

(72) Jahn, H. A.; Teller, E. Stability of Polyatomic Molecules in Degenerate Electronic States - I—Orbital Degeneracy. *Proc. Royal Soc. London A: Mathematical, Physical and Engineering Sciences* **1937**, *161*, 220–235.

(73) Ma, D.; Wang, Q.; Yan, X.; Zhang, X.; He, C.; Zhou, D.; Tang, Y.; Lu, Z.; Yang, Z. 3*d* Transition Metal Embedded C_2N Monolayers as Promising Single-Atom Catalysts: A First-Principles Study. *Carbon* **2016**, *105*, 463 – 473.

(74) Zheng, Z.; Wang, X.; Mi, W. Tunable Electronic Structure of Monolayer Semiconductor g-C_2N by Adsorbing Transition Metals: A First-Principles Study. *Carbon* **2016**, *109*, 764 – 770.

(75) Yu, S.; Rao, Y.-C.; Duan, X.-M. Modulating the Properties of Monolayer C_2N: A Promising Metal-Free Photocatalyst for Water Splitting. *Chin. Phys. B* **2017**, *26*, 087301.

(76) Zheng, Z.; Wang, X.; Mi, W. Tunable Electronic Structure and Spin Splitting in Single and Multiple Fe-Adsorbed g-C_2N with Different Layers: A First-Principles Study. *J. Phys. Chem. Solid.* **2018**, *115*, 221 – 227.

(77) Sahin, H. Structural and Phononic Characteristics of Nitrogenated Holey Graphene. *Phys. Rev. B* **2015**, *92*, 085421.

(78) Chakrabarty, S.; Das, T.; Banerjee, P.; Thapa, R.; Das, G. Electron Doped C_2N Monolayer as Efficient Noble Metal-Free Catalysts for CO Oxidation. *Appl. Surf. Sci.* **2017**, *418*, 92 – 98.

(79) Zhu, L.; Xue, Q.; Li, X.; Wu, T.; Jin, Y.; Xing, W. C_2N: an Excellent Two-Dimensional Monolayer Membrane for He Separation. *J. Mater. Chem. A* **2015**, *3*, 21351–21356.

View Article Online
DOI: 10.1039/C9CP03853A

Table 1: Electronic states of atom substitution in C_3N are specified as metal (M), half-metal (HM), ferromagnetic-metal (FM), spin-glass semiconductor (SG-SC), dilute-magnetic semiconductor (DM-SC) and semiconductor (SC). Band gap of semiconductors and the magnetic moment per super cell, are indicated inside parentheses. Direct and indirect band gap are specified as $-di$ and $-ind$, respectively.

Substitution site	H	O	S	F	Cl	B
C	M	SC (0.6 eV-*di*)	SC (0.33 eV-*ind*)	DM-SC ($1\mu_B$)	M	M
N	M	M	M	SC (0.8 eV-*di*)	SC (0.75 eV-*ind*)	SC(0.5 eV-*ind*)
Substitution site	C	Si	N	P	Li	Na
C	-	SC (0.34 eV-*di*)	M	M	M	FM (0.3)
N	M	M	-	M	M	SG-SC ($1.9\mu_B$)
Substitution site	K	Be	Mg	Ca	Al	-
C	M	M	M	FM (1.3 μ_B)	M	-
N	SG-SC ($2\mu_B$)	M	FM ($0.7\mu_B$)	HM ($1\mu_B$)	SC (0.43 eV-*di*)	-

View Article Online
DOI: 10.1039/C9CP03853A

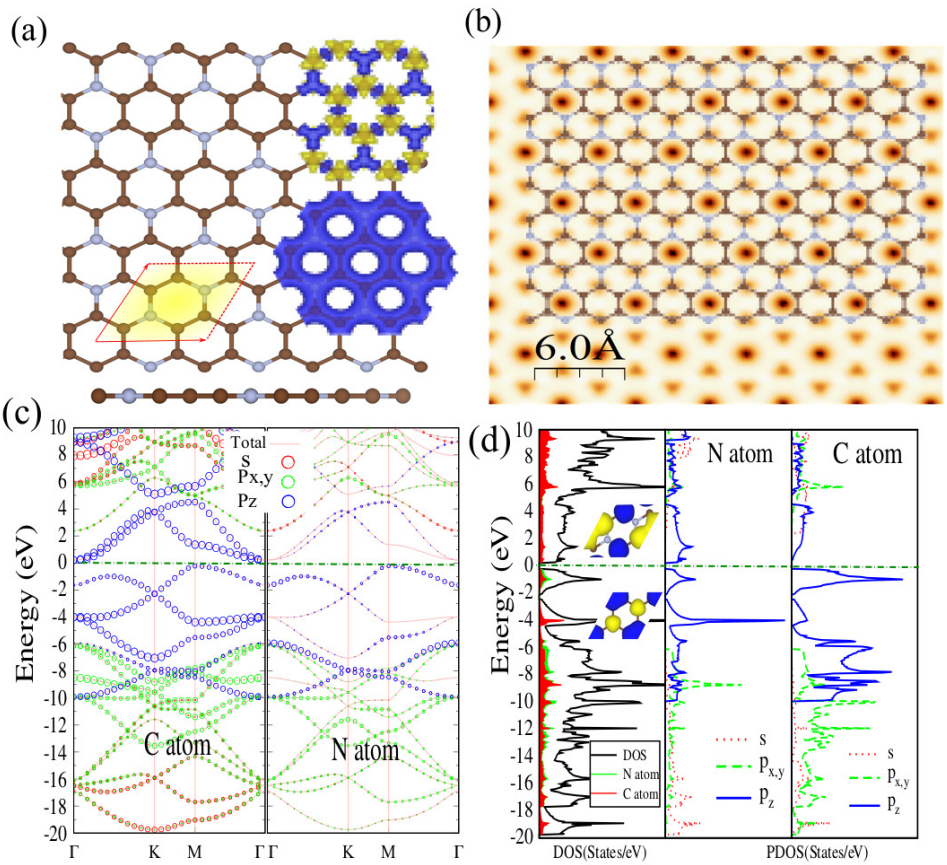

Figure 1: (a) Optimized atomic structure of C_3N, with its hexagonal primitive unit cell indicated by the red parallelogram. Gray (blue) balls are C (N) atoms. The total (bottom) and difference (up) charge density are also shown in the same panel. (b) Simulated STM image of C_3N overlayered with the C_3N lattice. (c) The orbital-projected and (d) electronic structure, DOS and PDOS. The charge distribution for the VBM and CBM are shown in the insets. Blue and yellow regions represent charge accumulation and depletion, respectively. The zero energy is set to the Fermi level energy (E_F).

View Article Online
DOI: 10.1039/C9CP03853A

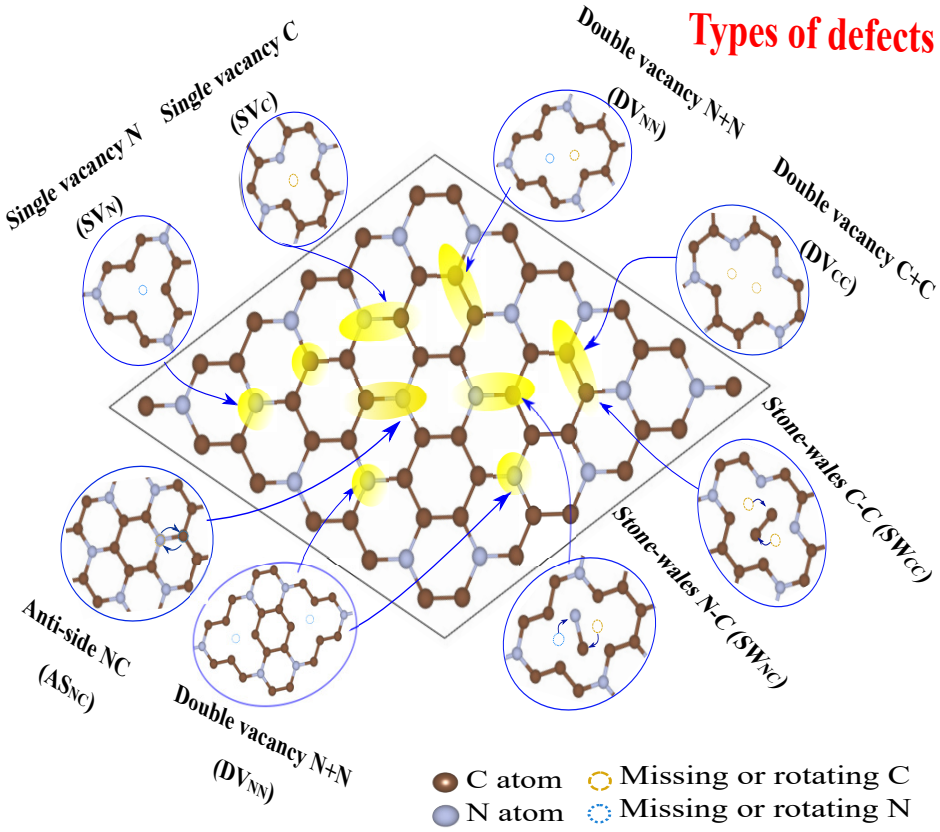

Figure 2: Schematic view of the different topological defects considered in the present paper: single vacancy with missing one C atom (SV_C), single vacancy with missing one N atom (SV_N), double vacancy with missing a pair of C (DV_{CC}), double vacancy with missing a pair of N (DV_{NN}), double vacancy with missing a pair of N and C (DV_{NC}), Stone-Wales (SW) and anti-site with exchange of the position of N and C atoms (AS_{NC}).

View Article Online
DOI: 10.1039/C9CP03853A

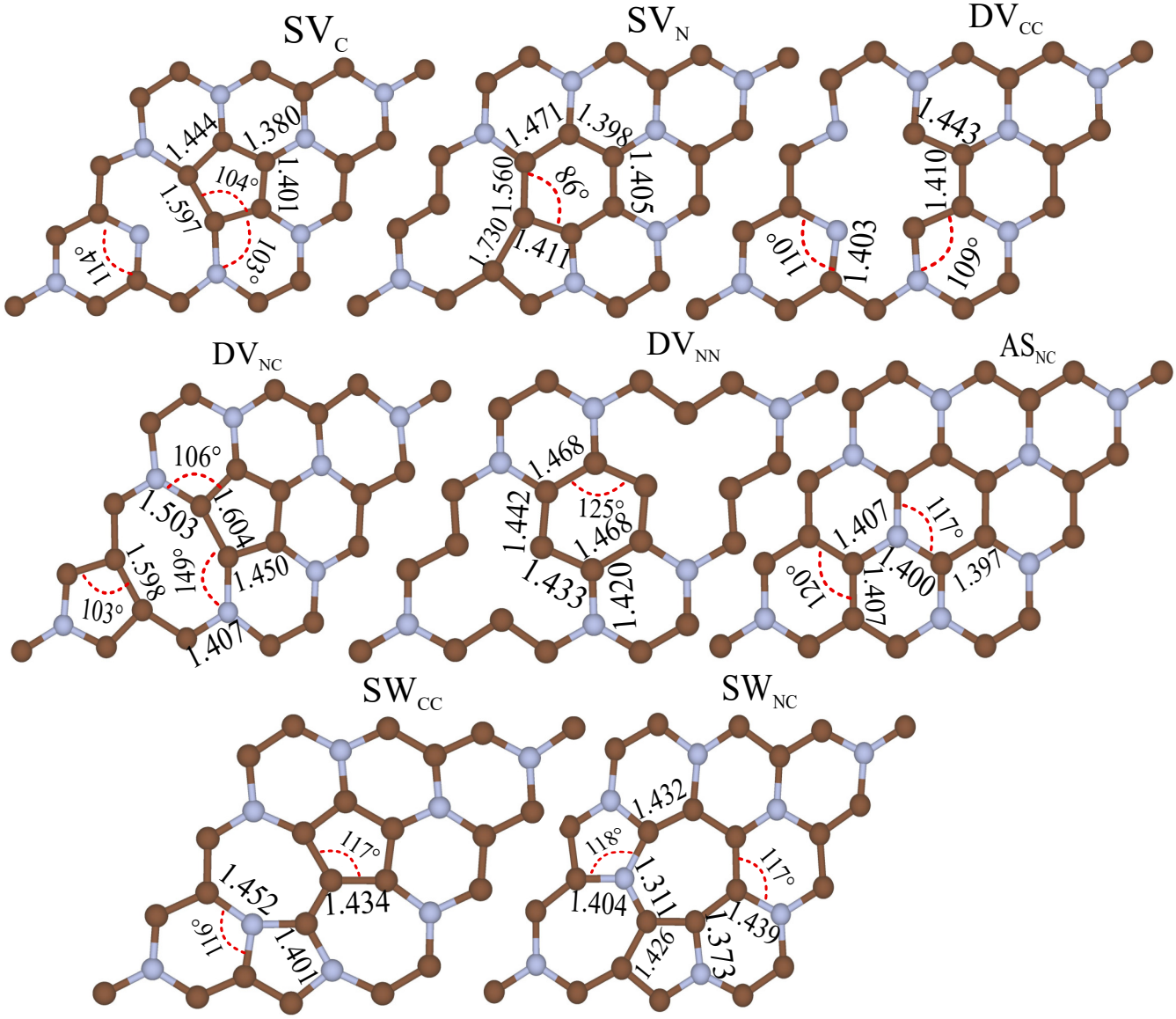

Figure 3: Optimized structures with corresponding bond lengths and angles of SV_C, (b) SV_N, C+C (DV_{CC}), N+C (DV_{NC}), N+N (DV_{NN}), anti-site (AS_{NC}), C-C (SW_{CC}) and N-C (SW_{NC}) defects on C_3N.

View Article Online
DOI: 10.1039/C9CP03853A

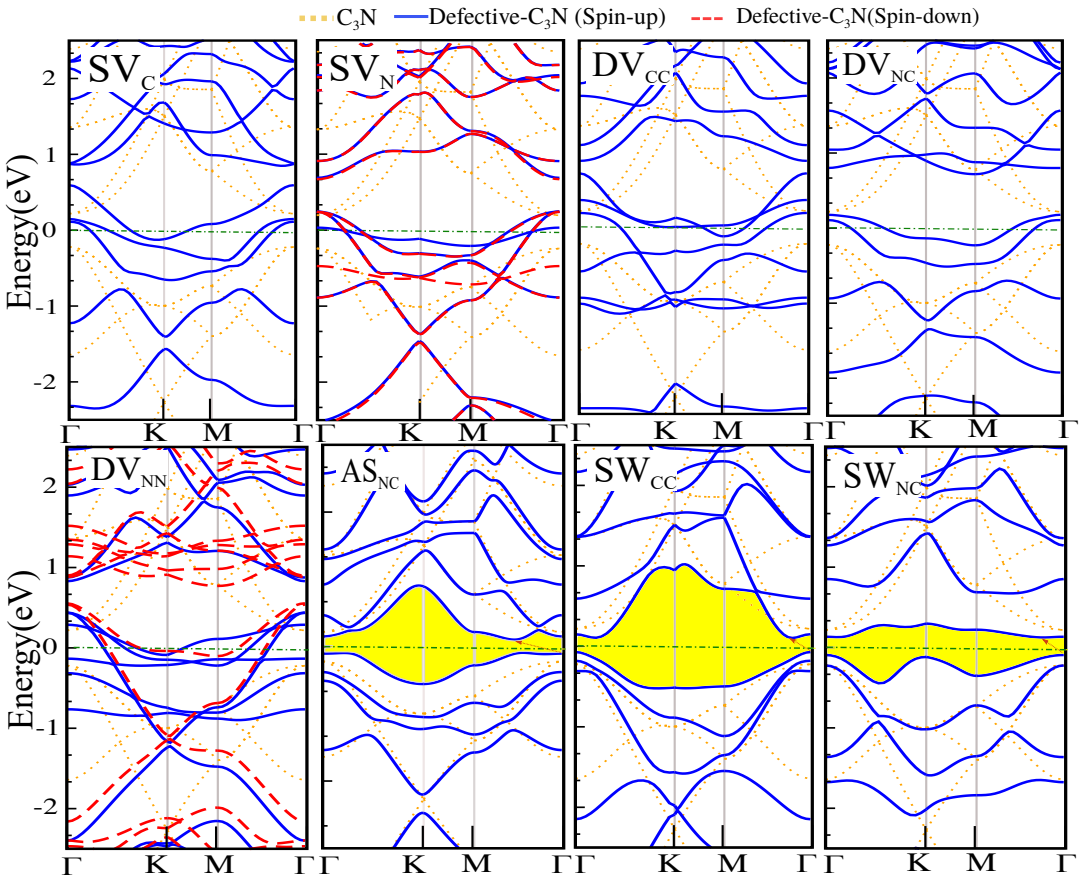

Figure 4: Effect SV_C, SV_N, C+C (DV_{CC}), N+C (DV_{NC}), N+N (DV_{NN}), anti-site (AS_{NC}), C-C (SW_{CC}) and N-C (SW_{NC}) defects on the electronic structure of C_3N. The dotted curves represent the electronic structure of pristine C_3N. The zero of energy is set to E_F, shown by the green dash-point line.

View Article Online
DOI: 10.1039/C9CP03853A

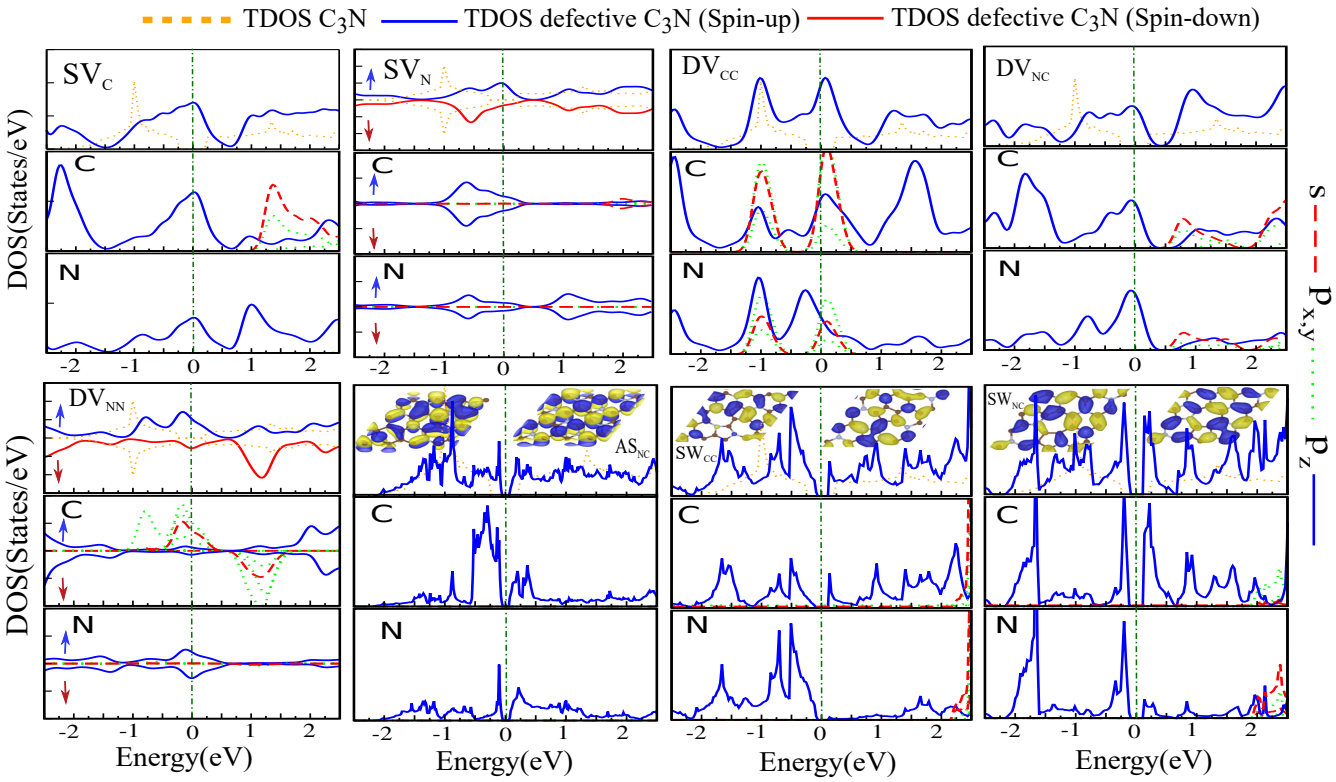

Figure 5: DOS and PDOS SV_C, SV_N, C+C (DV_{CC}), N+C (DV_{NC}), N+N (DV_{NN}), anti-site (AS_{NC}), C-C (SW_{CC}) and N-C (SW_{NC}) defects on C_3N. The charge distributions for the VBM and CBM are shown in the insets. Blue and yellow regions represent charge accumulation and depletion, respectively.

View Article Online
DOI: 10.1039/C9CP03853A

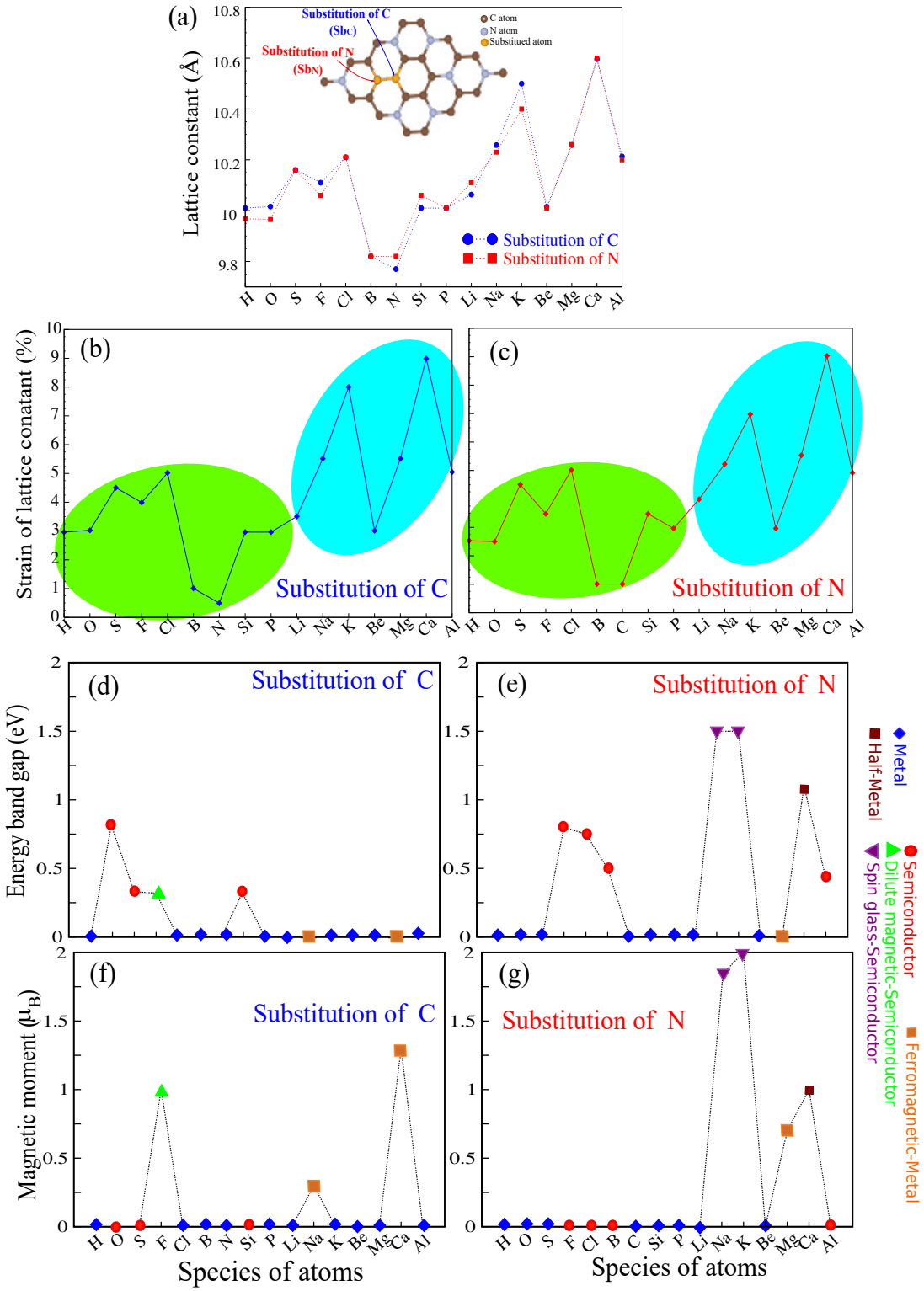

Figure 6: (a) Lattice constant of C_3N substituted with different atoms. Schematic model of two substitution sites is shown in the inset. (b,c) Effect of strain in lattice constant of C_3N substituted with different atoms. (d,e) Energy band gap and (f,g) magnetic moment due to substitution by difference species of atoms at respectively the, C and N host atom sites.

View Article Online
DOI: 10.1039/C9CP03853A

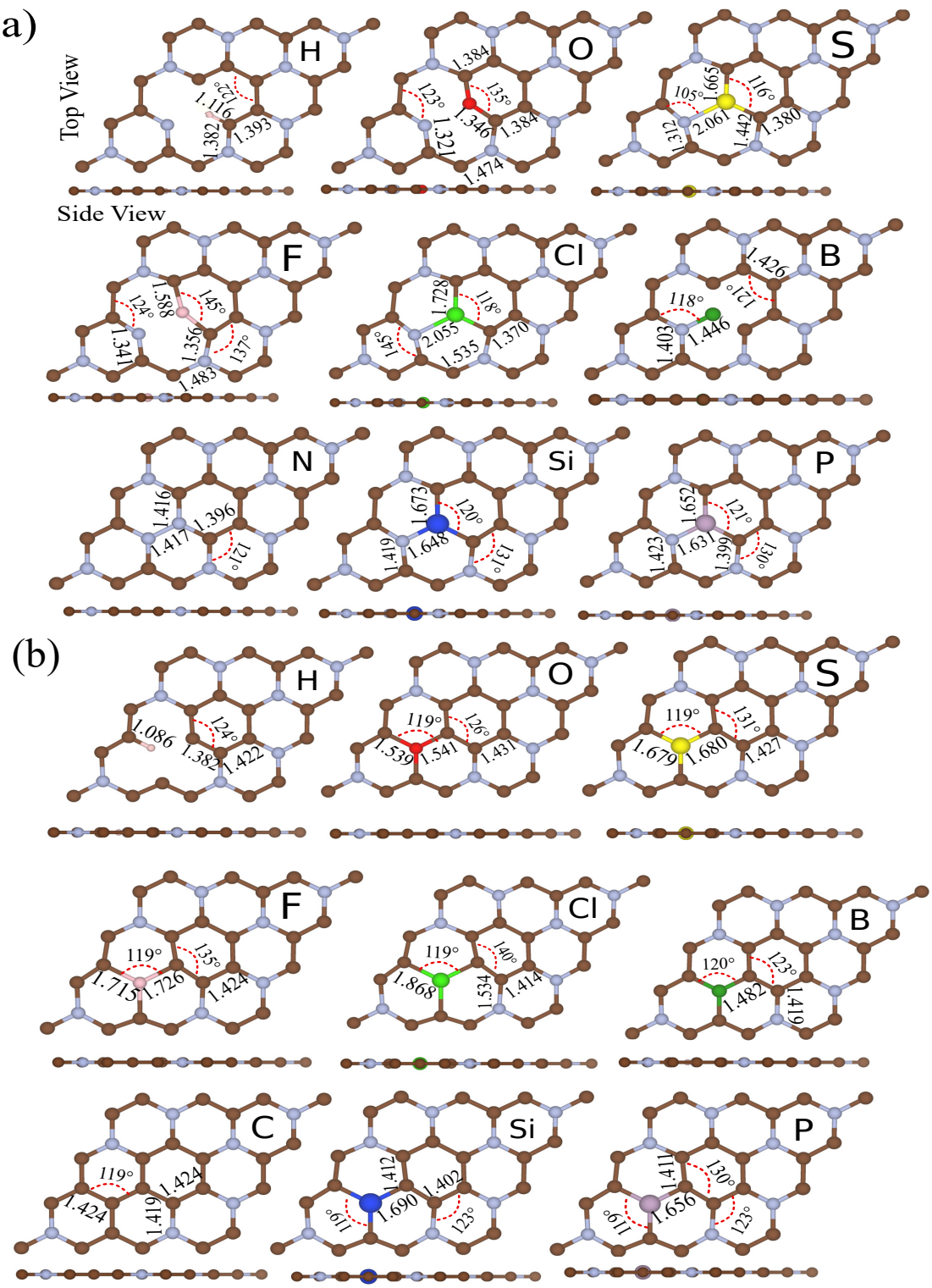

Figure 7: Optimized structures for substitution of (a) C or (b) N in the C_3N lattice with H, O, S, F, Cl, B, C, Si, N and P. Structural parameters including atomic bond length and angles are indicated. C, N and foreign atoms are shown by brown, blue and different colored balls, respectively.

View Article Online
DOI: 10.1039/C9CP03853A

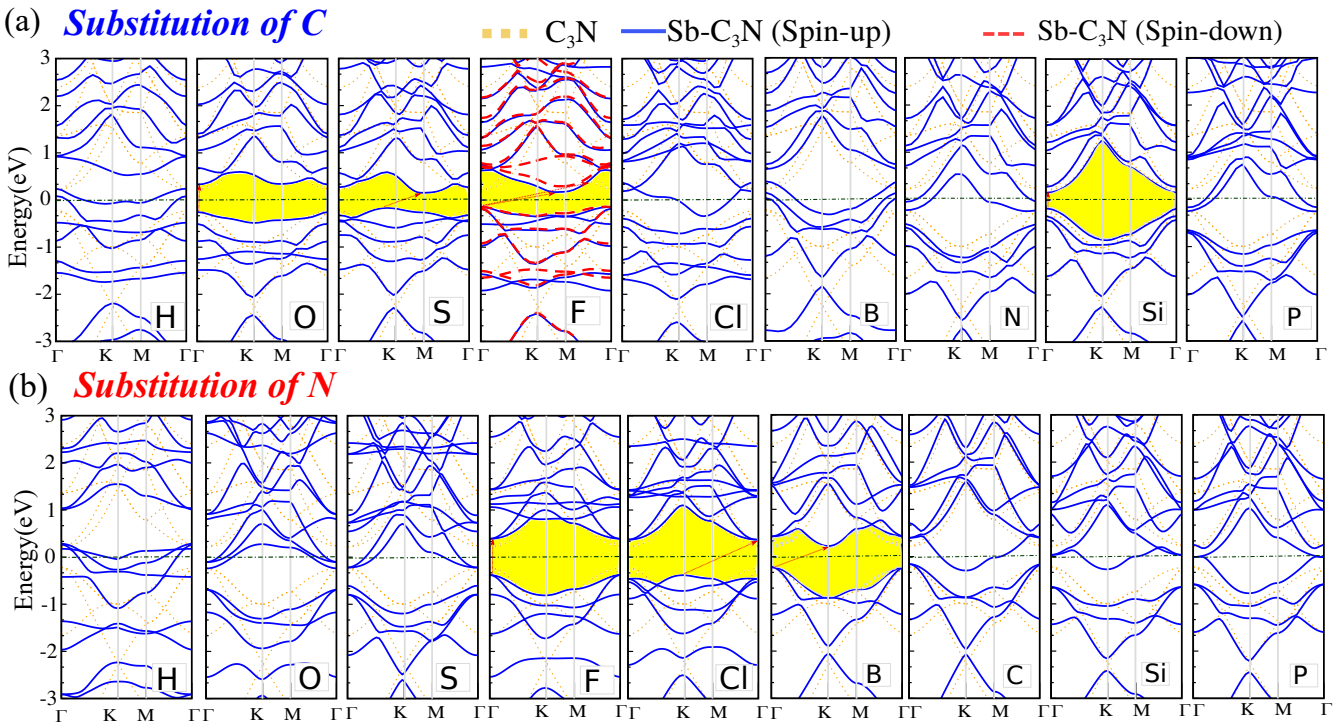

Figure 8: Electronic structure for substitution of (a) C or (b) N in the C_3N lattice with H, O, S, F, Cl, B, C, Si, N and P. The dotted curves represent the electronic structure of pristine C_3N. The zero of energy is set to E_F, shown by the green dash-point line.

View Article Online
DOI: 10.1039/C9CP03853A

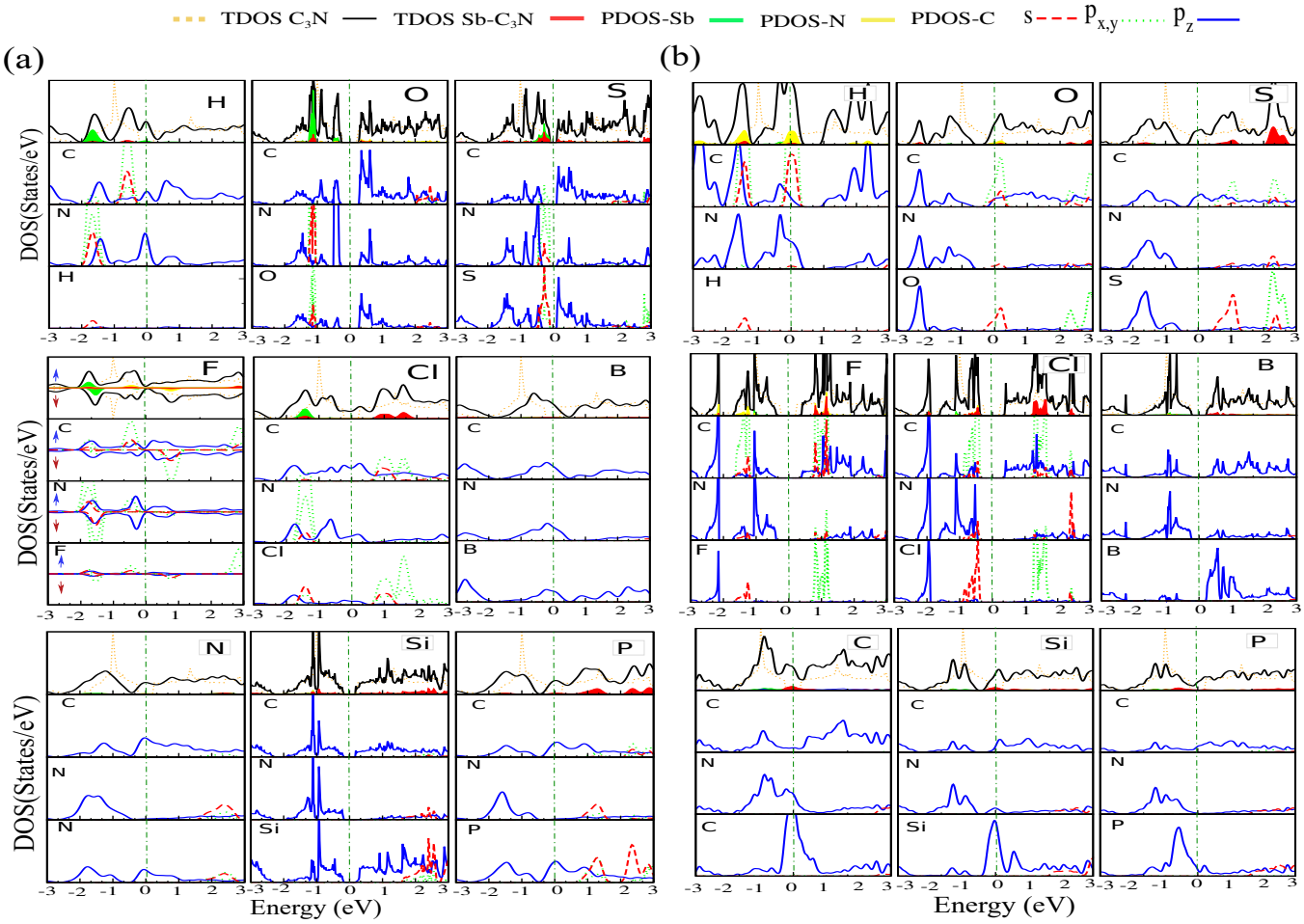

Figure 9: DOS and PDOS for substitution of (a) C or (b) N in the C_3N lattice with H, O, S, F, Cl, B, C, Si, N and P.

View Article Online
DOI: 10.1039/C9CP03853A

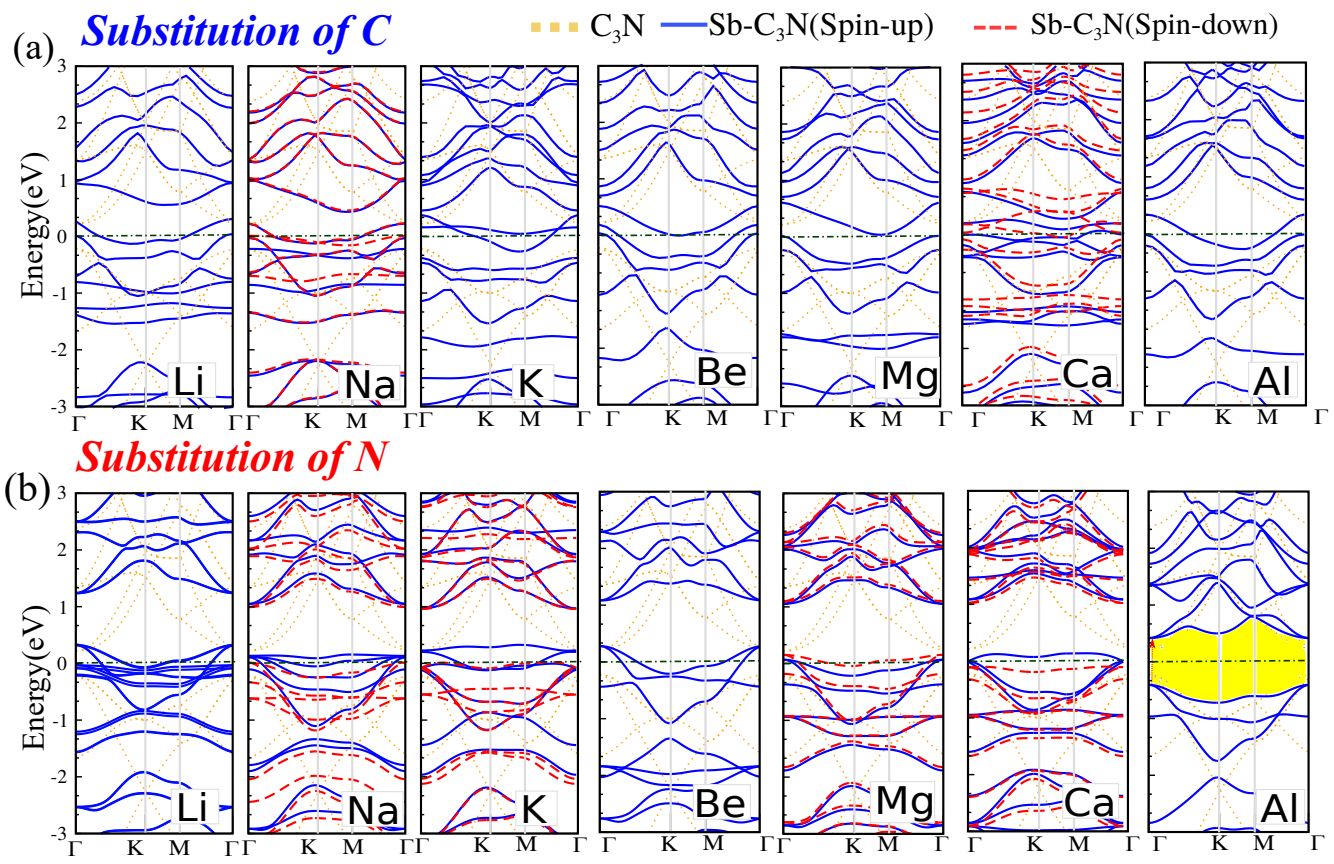

Figure 10: Electronic structure for substitution of (a) C or (b) N in the C_3N lattice with Li, Na, K, Be, Mg, Ca and Al. The zero of energy is set to E_F, shown by the green dash-point line.

View Article Online
DOI: 10.1039/C9CP03853A

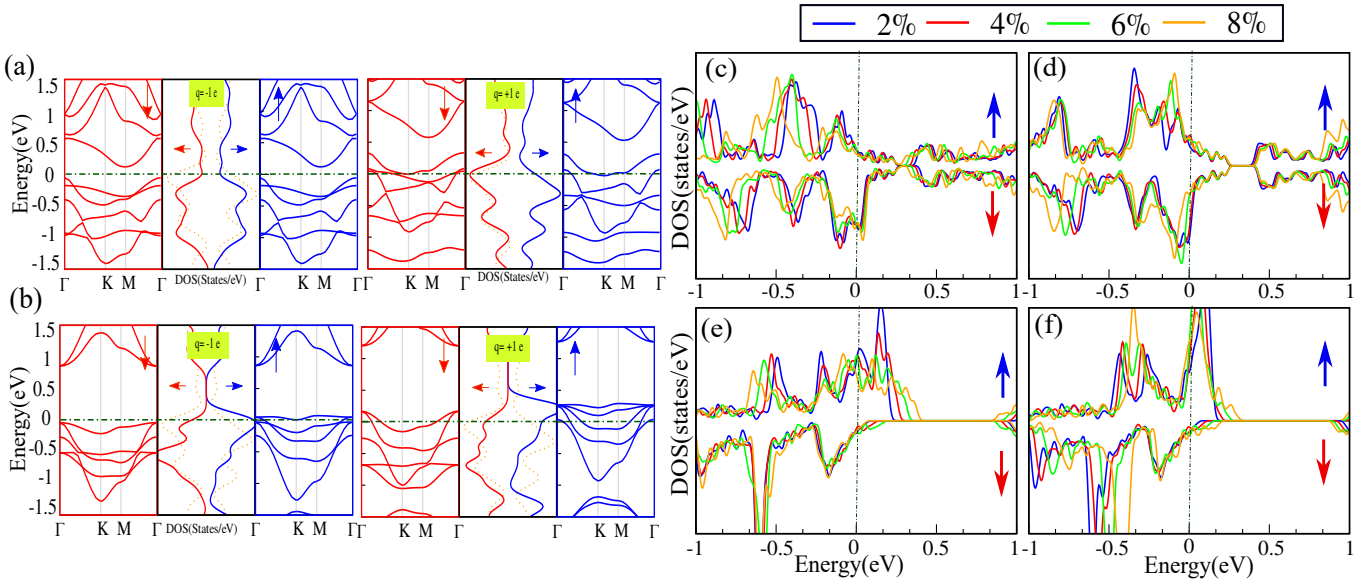

Figure 11: Electronic structure for two different values of the charging for Na substituted on (a) C and (b) N atom sites of C_3N. The DOS of Na substituted on (c,d) C and (e,f) N atom sites of the C_3N for different values of the uniaxial strain (tensile and compression). The q= +1 e and q= -1 e, corresponds to charging where one electron is removed from and add to the C_3N, respectively. The zero of energy is set to E_F, shown by the green dash-point line.

View Article Online
DOI: 10.1039/C9CP03853A

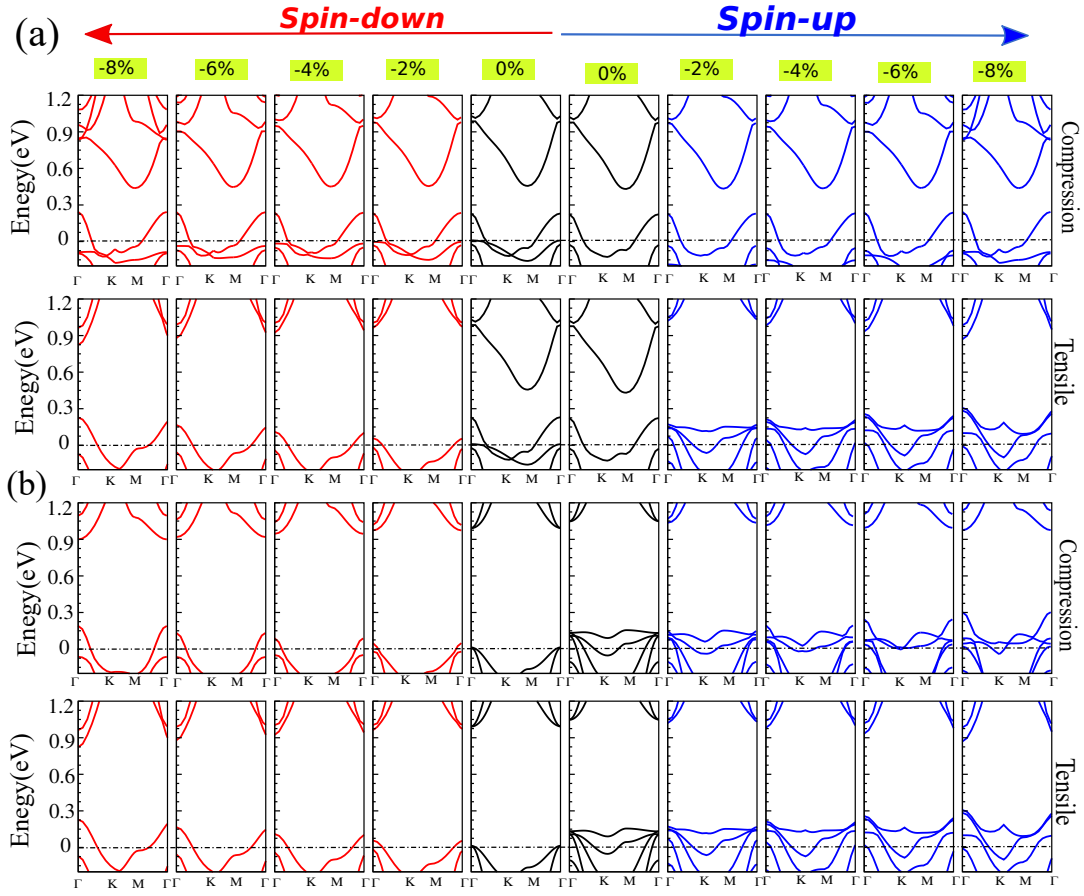

Figure 12: Electronic structures of Na substituted on (a) C and (b) N atom sites of C_3N for different values of strain. The zero of energy is set to E_F, shown by the green dash-point line.

View Article Online
DOI: 10.1039/C9CP03853A

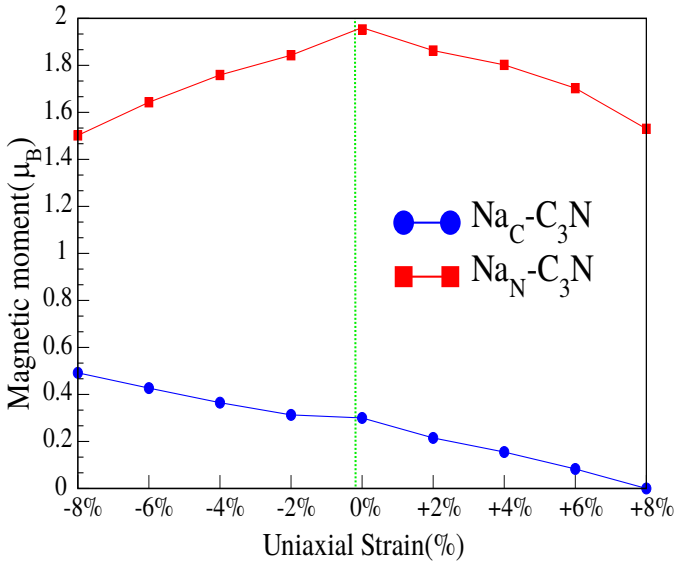

Figure 13: Magnetic moment of Na substituted C_3N as a function of strain.

View Article Online
DOI: 10.1039/C9CP03853A

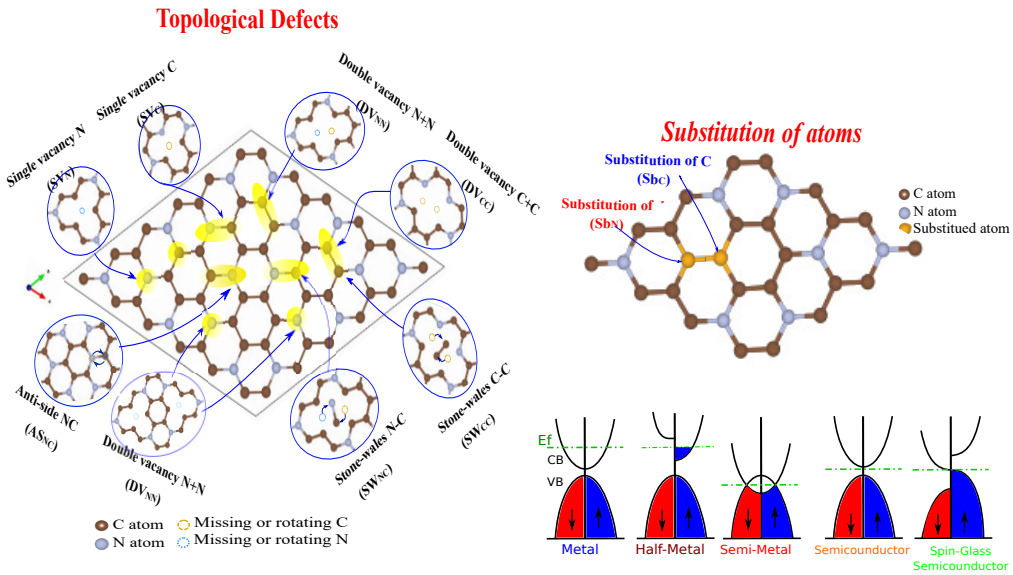

TOC